Geochimica et Cosmochimica Acta 364 (2024) 211–223

Contents lists available at ScienceDirect

Geochimica et Cosmochimica Acta

journal homepage: www.elsevier.com/locate/gca

Kinetic constraints for the formation of microniches for microaerophilic Fe (II) oxidation

S. Peiffer [a,*], M. Maisch [b], A. Kappler [b,c], C. Schmidt [b,1], M. Mansor [b], M. Obst [d], S. Frei [a,2]

[a] Hydrology, Bayreuth Center for Ecology and Environmental Science, University of Bayreuth, 95440 Bayreuth, Germany
[b] Geomicrobiology, Department of Geosciences, University of Tübingen, 72076 Tübingen, Germany
[c] Cluster of Excellence: EXC 2124: Controlling Microbes to Fight Infection, Tübingen, Germany
[d] Experimental Biogeochemistry, Bayreuth Center for Ecology and Environmental Science, University of Bayreuth, 95440 Bayreuth, Germany

ARTICLE INFO

Associate editor: Juan Liu

ABSTRACT

Oxidation of Fe(II) by oxygen (O_2) at circumneutral pH occurs abiotically or is mediated by microaerophilic Fe (II)-oxidizing bacteria. Abiotic Fe(II) oxidation(s) compete with microbial processes and the relative contribution of abiotic reactions depend on the chemical conditions, e.g. P_{O2}, pH and the presence and identity of ferric (oxyhydr)oxide mineral surfaces, catalyzing the heterogeneous reaction. At circumneutral pH, abiotic Fe(II) oxidation proceeds rapidly, which raises the question how and to which extent neutrophilic microaerophilic Fe (II)-oxidizing bacteria can compete with chemical reactions and gain metabolic energy from microbial Fe(II) oxidation. In this study, we have investigated the environmental constraints for microaerophilic Fe(II) oxidation in a film layer characterized by diffusive supply of both atmospheric O_2 (from the top) and dissolved Fe(II) (from the bottom) by use of a numerical model. A coupled diffusion–reaction model was tested at different chemical (pH and alkalinity gradients) and physical (film layer thickness) parameters to investigate their effects on the relative contributions of different reactions (abiotic homogeneous, heterogeneous and biological Fe(II) oxidation) to the overall (net) Fe(II) oxidation. A first order rate constant for biological oxidation was derived from experimental data from simplifcation of a Monod rate law to be 0.06 h^{-1}. The simulations demonstrate distinct spatial oxidation rate patterns for all of the considered reactions. Microaerophilic Fe(II) oxidation is predominant at a uniform pH 6 and a film thickness z of 1 mm with minor importance at pH 7. Maximum biological rates were on the order of $7 \bullet 10^{-10}$ mol L^{-1} s^{-1} and are in the range of experimentally observed values. Minimum rates were close to the thermodynamic limit. In the presence of a pH gradient and $z \leq 1$ mm, two distinct zones were observed: an upper zone dominated by abiotic Fe(II) oxidation (pH ~ 7) and a lower zone dominated by microaerophilic Fe(II) oxidation (pH < 6.3), while the position and extent of the zones depend on the alkalinity. Such separation is strongly amplified for thinner films ($z = 0.2$ mm). The importance of heterogenous oxidation depends both on the pH and the amount of ferric (oxyhydr)oxides formed which increases with decreasing diffusive O_2 supply at $z > 1$ mm. In combination with high resolution imaging of pH values in a biofilm, our simulations underpin the importance of pH gradients in allowing for the formation of microniches. The conditions suitable for microaerophilic Fe(II) oxidation can be predicted based on reaction time scales and three factors were identified to be especially important: i) a pH low enough (<6.3) to outcompete abiotic processes; ii) sufficiently fast diffusive supply of Fe(II) (e.g. by Fe(III)-reducing bacteria or chemical processes) with O_2 concentrations below 150 μmol L^{-1}; iii) sufficient energy gain from Fe(II) oxidation reaction considering the thermodynamic factor F_T. We end by discussing strategies that Fe(II)-oxidizing microorganisms can employ to enhance their competitiveness against abiotic reactions.

* Corresponding author at: Universitätsstrasse 30, 95440 Bayreuth, Germany.
E-mail address: s.peiffer@uni-bayreuth.de (S. Peiffer).
[1] Now: AI Research Building (TTR2), University of Tübingen, 72076 Tübingen.
[2] Now: Aquatic Ecology and Water Quality Management Group, Department of Environmental Science, Wageningen University Research Centre, 6700 AA Wageningen, The Netherlands.

https://doi.org/10.1016/j.gca.2023.11.006
Received 10 June 2023; Accepted 6 November 2023
Available online 8 November 2023

1. Introduction

Abiotic oxidation of dissolved Fe(II) at circumneutral pH is a rapid process that is able to lower initial Fe(II) concentrations at pH 7 and atmospheric O_2 concentration by a factor of 100 within ~ 3 h (Stumm and Morgan, 1996). Nevertheless, a large variety of microorganisms exist that are able to harvest energy from oxidation of Fe(II) with O_2 as the terminal electron acceptor at circumneutral pH, albeit growth and metabolic activity under these conditions appears to be a challenge (Emerson, 2012; Kappler et al., 2021; Neubauer et al., 2002). The energy gain from enzymatic Fe(II) oxidation coupled to O_2 reduction is low (Ehrlich et al., 1991) and doubling times for these Fe(II)-oxidizing bacteria are reported to be longer than 8 h (Emerson and Moyer, 1997; Hädrich et al., 2019; Maisch et al., 2019) and even up to 27 h for marine species (Chiu et al., 2017). Hence, such iron(II)-oxidizing bacteria must either successfully compete with rapid abiotic processes governing Fe(II) oxidation, or find suitable niches with geochemical parameters favouring their physiological needs. Despite this, it was demonstrated that biological Fe(II) oxidation coupled to O_2 reduction can contribute by up to 53 % to the total Fe(II) oxidation in wetland rhizosphere batch cultures (Neubauer et al., 2002), which in turn highlights their relevance to the oxidative side of the iron cycle in environmental settings.

A solution for bacteria to survive under such harsh conditions is a microaerophilic lifestyle. So-called microaerophilic Fe(II)-oxidizing bacteria have adapted to primarily inhabit low-O_2 environments where they can successfully compete with abiotic Fe(II) oxidation (Druschel et al., 2008). Several microorganisms were found to be able to oxidize Fe(II) at low micromolar O_2 concentrations, when abiotic Fe(II) oxidation kinetics slow down substantially (Chan et al., 2016). Maintenance of microoxic conditions, however, requires a physical setting in which low micromolar concentrations of dissolved O_2 are controlled by a combined diffusive O_2 supply from the atmosphere and concomitant consumption (by chemical or biological O_2 reduction reactions) along the diffusion path. This is a situation typically found in sediments or in a microbial biofilm in which on the one hand continuous Fe(II) supply exists, e.g. from reductive dissolution of Fe(III) (oxyhydr)oxides, and on the other hand some biogeochemical processes are present to reduce O_2 concentrations to appropriate micromolar levels (Schmidt et al., 2010; Sobolev and Roden, 2001).

Abiotic Fe(II) oxidation occurs in both homogeneous and heterogeneous reactions. Homogeneous Fe(II) oxidation kinetics primarily depends on O_2 concentrations but is also extremely sensitive to pH conditions. The homogeneous oxidation rate decreases by a factor of 100 from pH 7 to pH 6 (Stumm and Morgan, 1996). Meanwhile, surface-catalysed heterogeneous Fe(II) oxidation (i.e. the oxidation of Fe(II) adsorbed to ferric (oxyhydr)oxide surfaces) is less sensitive to pH with a decrease in oxidation rates by a factor of only 10 from pH 7 to pH 6 (Tamura et al., 1976). The cause for these differences is related to the chemical speciation of Fe(II). In heterogeneous Fe(II) oxidation, the reaction is surface catalysed and pH dependence is related to the extent of adsorption of Fe(II) on the ferric (oxyhydr)oxides surface. The sorption edge decreases between pH 7 and 6 from ~ 90 % to ~ 10 % adsorption, respectively (Dixit and Hering, 2006). In contrast, the pH dependency of microaerophilic Fe(II) oxidation by bacteria is poorly known. For example, neutrophilic Fe(II)-oxidizing bacteria isolated from the rhizosphere of wetland plants were shown to grow between pH 4.5 and 7.0 with no growth observed at pH 8.0 (Weiss et al., 2007), suggesting that slightly acidic (pH < 7.0) environments can favour the abundance and activity of these organisms. However, in the marine environment, there are some Fe(II)-oxidizers that have been shown to grow up to pH 8.3, though their optima are much lower (Chiu et al., 2017).

The available knowledge therefore suggests that pH, on top of O_2, is an important parameter for the development of microniches that are suitable to microaerophilic Fe(II)-oxidizing microorganisms (Druschel et al., 2008). However, little is known about the actual formation and presence of such micro-niches within an Fe(II)-oxidizing (bio-)film layer. A kinetic model predicting such niches under variable boundary conditions (pH, O_2, layer thickness) is still missing in the field of Fe biogeochemistry.

In this study, we have investigated the environmental constraints for microaerophilic Fe(II) oxidation by use of a numerical model simulating a film layer characterized by diffusive supply of both atmospheric O_2 from the top and dissolved Fe(II) from the bottom. We hypothesize that suitable geochemical conditions established within such a film layer will allow for the activity of microaerophilic Fe(II)-oxidizing bacteria by promoting biological over abiotic Fe(II) oxidation. We used reference data for abiotic Fe(II) oxidation kinetics and derived a kinetic model for microaerophilic Fe(II) oxidation based on parameters obtained from incubation experiments under varying microoxic conditions (Maisch et al., 2019). Simulation results were evaluated using a spatial analysis of pH gradients in a Fe(II)-oxidizing, alkalinity-rich biofilm by means of confocal laser scanning microscopy.

2. Methods

2.1. Conceptual model for an Fe(II)-oxidizing oxic-anoxic interface

Given the strong pH dependency of abiotic Fe(II) oxidation kinetics, it is obvious to start by investigating the effect of pH on the spatial distribution of the various Fe(II) oxidation pathways. Gradients of pH typically exist at diffusion-controlled film layers such as sediment–water interfaces (e. g. Sobolev and Roden, 2001; Kappler et al., 2004; Rubin-Blum et al., 2014), biofilms (Kappler et al., 2004; Kühl and Jørgensen, 1992; Peiffer et al., 2021) and microbial mats (Kühl and Jørgensen, 1992). Typically, higher pH is observed on the oxic side of the interfacial layer (Cai et al., 1995; Kühl and Jørgensen, 1992; Rubin-Blum et al., 2014). Upon oxidation of Fe(II), the formation of Fe(III) (oxyhydr)oxides acidifies the environment, which can lead to the development of pH gradients (Sobolev and Roden, 2001) as controlled by the alkalinity (i.e. buffer capacity) within the interfacial zone. In addition to such chemical controls, pH gradients are also controlled by the diffusion velocity within the film layer, which in turn depends on the layer thickness. Thicknesses of redox interfaces may vary from the submicrometer scale (Peiffer et al., 2021) to a few centimeters (Emerson and Weiss, 2004).

Environmental interfaces are often characterized by strong redox gradients. Within such gradients, numerous bacterial species can benefit from stepwise redox reactions and often find a suitable niche that harbours optimum conditions for their metabolism (Reyes et al., 2016). For our simulations, in order to quantify the contribution of biological Fe(II) oxidation to Fe(II) removal, we have adopted the conceptual model of an anoxic–oxic interface (Sobolev and Roden, 2001) which we in the following denote as the biofilm model (Fig. 1).

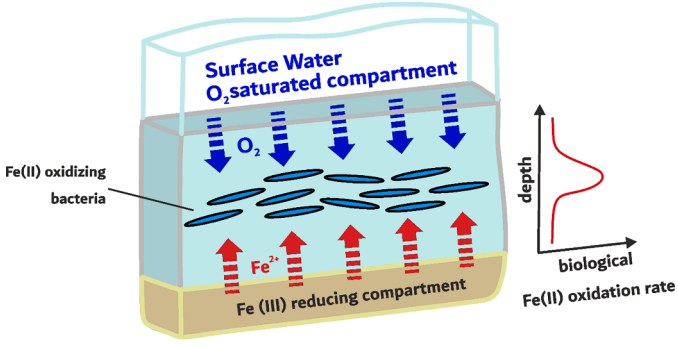

Fig. 1. Conceptual model of a (bio)film layer being in contact with an Fe(II) generating layer at the bottom and an oxygen saturated layer at the top. Biological rates are expected to be highest at the optimum depth.

We assume a one-dimensional vertical distribution of O_2 and Fe(II) shaped only by Fe(II) oxidation and diffusive reactant transport. We did not consider microbial aerobic O_2 consumption which would substantially enhance complexity such as making assumptions about autotrophic organic matter production and O_2 threshold values of respiratoric oxygen uptake. In the following text we use the notation Fe(II) to account also for ionic Fe^{2+} (cf. SI 1 for further explanations).

The biofilm is supplied with a constant flux of Fe(II) originating from a compartment adjacent to the bottom of the biofilm. Such a supply exists in nature as result of reductive dissolution of Fe(III) minerals in the deeper layer and is regarded to be part of a microscale bacterial Fe redox cycle at the oxic-anoxic interface (Roden et al., 2004). The concentration of Fe(II) at the upper end of the biofilm is zero, and inversely, O_2 concentration at the upper end is at equilibrium with the atmosphere, while no dissolved O_2 is available at the lower end of the biofilm due to chemical or biological reactions reducing (in other words: consuming) O_2 within the film layer as it was observed before (Lueder et al., 2018).

Boundary conditions selected are: i) a constant flux of $3.17 \bullet 10^{-12}$ mol cm^{-2} s^{-1} Fe(II) at the lower end of the biofilm, e.g. from microbial reduction of ferric (oxyhydr)oxides. This value corresponds to a net production rate of ~ 250 nmol Fe(II) cm^{-3} d^{-1} (e. g. Peine et al., 2000) in a volume of 1 cm thickness. ii) a constant concentration of Fe(II) at the upper end (c(Fe(II)) = 0 mol L^{-1}), iii) a constant O_2 concentrations at the upper end of the biofilm (equilibrium with the atmosphere, 0.27 mmol L^{-1} at 25 °C) and at its lower end ($c(O_2)$ = 0 mol L^{-1}). The virtual biofilm model was implemented in the MATLAB environment and accounts for biological, abiotic homogeneous and abiotic heterogeneous oxidation rates of Fe(II) (R_{bio}, R_{homo}, and R_{hetero}, resp., SI section 1).

The variables considered in the simulations are biofilm thickness and temperatures, alkalinity gradients to account for buffer capacity against proton generation (due to Fe(II) oxidation and the subsequent precipitation of Fe(III) (oxyhydr)oxides) as well as pH gradients. In addition, we considered conditions of uniform pH values within the biofilm. Within the biofilm, only diffusive transport occurs. All simulation plots presented reflect steady-state conditions (cf. SI section 1). Table 1 summarizes the various simulation scenarios with corresponding chemical boundary conditions, biofilm thicknesses and temperatures.

Table 1
Overview about the simulated scenarios.

Simulation scenario #	Film Thickness (mm)	T (°C)	Boundary	pH	Alkalinity (mmol L^{-1})	TIC (mmol L^{-1})
#1 Constant pH, constant alkalinity and equilibrium with atmosphere						
#1a, pH = 7.0	1	25	Upper	7	4.1	4.1
			Lower	7	4.1	5.0
#1b, pH = 6.25	1	25	Upper	6	2.3	2.3
			Lower	6	2.3	5.0
#1c, pH = 6.0	1	25	Upper	6	1.7	1.7
			Lower	6	1.7	5.0
#2 pH gradient in biofilm, constant total inorganic carbon (TIC) or Alkalinity						
#2a, TIC = 5 mmol L^{-1}	1	25	Upper	7	4.1	5.0
			Lower	6	1.7	5.0
#2b, Alk = 1.7 mmol L^{-1}	1	25	Upper	7	1.7	1.7
			Lower	6	1.7	5.0
#3 Variation of film thickness						
#3a: Biofilm thickness 0.2 mm; chemical conditions as in #1a	0.2	25	Upper	7	4.1	4.1
			Lower	7	4.1	5.0
#3b: Biofilm thickness 0.2 mm; chemical conditions as in #1b	0.2	25	Upper	6	1.7	1.7
			Lower	6	1.7	5.0
#3c: Biofilm thickness 0.2 mm; chemical conditions as in #2b	0.2	25	Upper	7	1.7	1.7
			Lower	6	1.7	5.0
#3d: Biofilm thickness 5 mm; chemical conditions as in #2b	5	25	Upper	7	1.7	1.7
			Lower	6	1.7	5.0
#3e: Biofilm thickness 30 mm; chemical conditions as in #2b	30	25	Upper	7	1.7	1.7
			Lower	6	1.7	5.0
#4 Variation of temperature						
Chemical conditions as in #2b	1	10	Upper	7	1.7	1.7
			Lower	6	1.7	5.0

2.2. Confocal laser scanning microscopy study of an Fe(II)-oxidizing biofilm

2.2.1. Microscopic pH distribution

A sample of a microaerophilic Fe(II)-oxidizing biofilm was taken from a concrete-covered wall of the Erwein II iron mining tunnel in Pegnitz, Germany on February 16th 2022. It was analysed for microscale pH distribution on February 17th, and for the distribution and composition of extracellular polymeric substances (EPS) and associated Fe(II) on February 21st 2022. The sample was stored dark in the original sample water at 2 °C until analysis.

The microscale pH distribution was determined by ratiometric imaging. To this end, 100 µL aliquots of the biofilm sample in original sample water were stained with 1 µL of a 1:5 aqueous dilution of Syto40™ blue fluorescent DNA stain (Thermo Fisher) to localize cells and 2 µL of the ratiometric pH sensitive fluorescence stain SNARF 4F™ (Thermo Fisher) in its not cell-permeable form of the carboxylic acid for 20 min. An 8 µL aliquot of the stained sample was pipetted into a SecureSeal™ imaging spacer and immediately covered with a cover slip. The samples were analysed in an upright Leica SPE confocal laser scanning microscope equipped with an ACS APO 63x water immersion lens with a numerical aperture of 1.15. All images were recorded with a pinhole size of 1 Airy unit, a lateral pixel spacing of 0.11 µm and a Z stepsize of 0.388 µm.

The ratiometric pH stain was excited with a 561 nm laser and images were recorded in the ranges of 571–610 nm and 620–700 nm, respectively. Laser intensities, PMT voltages and channel accumulation factors were adjusted for optimum signal noise ratios to achieve intensity histograms for both channels that are entirely within the dynamic range without touching the upper or lower limit. Accumulation factors were considered in the subsequent calculation of the image ratios.

All image processing was done using the Fiji software package (Schindelin et al., 2012). To reduce pixel noise, a gaussian blur filter of σ = 0.5 µm was applied to both channels. pH values were then calculated from the ratio of the intensities of the two image stacks upon calibration in the pH range of 4.5–7.0 in steps of 0.5 pH units.

The DNA stain was excited with a 405 nm laser and the emission was recorded in a range from 420 to 480 nm. The reflected signal of the 488 nm laser was used to localize all structures of the biofilm such as the twisted stalks.

For identification of acidic regions, the mean pH for the entire measurement volume (~530,000 μm^3) was calculated. Based on the pH histogram (Fig. 8b, horizontal greyscale histogram), a negative deviation of each respective voxel of > 0.2 pH units was considered "acidic".

For the identification of cells, a threshold of 19 was applied to the DNA channel to separate signal from background noise. A map of the cells with acidic microenvironment was derived by back-mapping of the light red marked region in Fig. 8b by using the ImageJ plugin ScatterJ

(Zeitvogel et al., 2016). The obtained mask was multiplied with the DNA signal to derive a 3D map of the cells with acidic microenvironment shown in red in Fig. 8a, whereas all other cells are shown in the blue channel of Fig. 8a.

The volume fraction occupied by cells was calculated from the deconvoluted dataset upon applying a gaussian blur filter of $\sigma = 0.25$ µm for noise reduction and the default threshold method for segmentation. The acidic volume fraction was calculated using a threshold value on the 3D pH dataset equivalent to a pH value of 0.2 units below the mean pH value of the entire dataset. Volume fraction calculations were done using the statistic functions of Fiji.

2.2.2. Microscopic Fe(II) distribution within EPS

The distribution of Fe(II) was measured in the same biofilm sample as described for the pH measurements. The staining of the sample followed the procedure described by (Hao et al., 2016), using the lectin-dye conjugates SBA-Alexa Fluor 635, PNA-Alexa Fluor 568 for EPS staining, Fe(II) sensor 2 and the DNA fluorescent stain Syto^{TM} 40. The following amounts of stains were added to a 100 µL aliquot of biofilm in original sample water: 1 µL of each of the lectin-dye conjugates at a concentration of 1 mg/mL in deionized water, 4 µL of Syto^{TM} 40 (1:5 aqueous dilution) and 4 µL of Fe(II) sensor 2. The samples were acquired in the same instrument as described previously using a 635 nm laser for the SBA-Alexa Fluor 635 channel, a 561 nm laser for the PNA-Alexa Fluor^{TM} 568 channel, a 488 nm laser for the Fe(II) sensor 2 and a 405 nm laser for the Syto^{TM} 40 channel. The 3D datasets were analysed for correlations using the Fiji plugin ScatterJn (Zeitvogel and Obst, 2016).

3. Results

3.1. Concentration gradients within the film layer

In simulations with a film thickness < 5 mm, concentration gradients of oxygen were linear and identical, irrespective of the scenarios. Such linear gradients correspond to a diffusive oxygen flux across the film of $2.7 \bullet 10^{-9}$ mol cm^{-2} s^{-1} at 25 °C ($c(O_2)$ at saturation is 0.27 mmol L^{-1}) and a film thickness of 1 mm, which is roughly 3 orders of magnitude higher than the Fe(II) flux of $3.17 \bullet 10^{-12}$ mol cm^{-2} s^{-1} used in the simulations. Only at at film thickness of 30 mm, a slight deviation from this linear pattern could be observed (Fig. S3). The oxygen concentration gradient follows oxygen uptake processes in the anoxic zone underlying the Fe(II)-oxidizing layer (Fig. 1) from a variety of oxygen consuming processes. Based on Fick's 1st law, oxygen fluxes scale with film thickness. However, even at the thickest film considered (30 mm), the flux is still relatively high at $9 \bullet 10^{-11}$ mol cm^{-2} s^{-1} compared to the Fe(II) flux. Apparently, the Fe(II) oxidation rates do not affect the overall O_2 flux substantially in the scenarios considered. In contrast, Fe(II) concentration profiles clearly depend on the specific scenario and the depth of the film (Fig. 2). At a constant pH, the gradient decreases from the bottom to the upper end at a thickness of 1 mm while it is linear at a thickness of 0.2 mm (at pH 6, the pattern is identical, data not shown). In the scenarios simulated with a pH decreasing from the upper end (pH 7) to the lower end (pH 6), gradients are generally linear, except in scenarios 3d and 3e, in which film thickness was 5 and 30 mm, respectively. Under these conditions, the gradient increases towards the upper end. Fe (II) was already completely consumed at the center of the film in scenario 3e (30 mm thickness). Following the dependence of O_2 fluxes on film thickness, the concentration of Fe(II) at the lower boundary also scales with film thickness with a higher concentration at thicker films.

pH gradients in these scenarios underpin the importance of alkalinity (Fig. S4a). At constant alkalinity, the pH slightly decreases in the upper end of the film with the gradient strongly increasing towards the bottom. If total inorganic carbon (TIC) is kept constant, which is equivalent to a higher alkalinity at the upper end as compared to the lower end of the film layer (Fig S 3b), the pH drop is almost linear.

3.2. Scenario #1: Spatial distribution of Fe(II) oxidation rates at a constant pH within the biofilm

In this scenario, we have simulated Fe(II) oxidation rates for conditions at which pH is constant throughout the biofilm. pH measurements performed in biofilms reflect slightly acidic to neutral pH values (Peiffer et al., 2021) so that we have selected pH 7 and pH 6 for our scenarios to mimic circumneutral conditions. Biofilm thickness was set to 1 mm. TIC was set to 5 mmol/L at the lower end and equilibrium with atmospheric CO_2 ($P_{CO2} = 0.0004$ atm) at the upper end. We further assumed that alkalinity is maintained in the biofilm so that we obtain TIC values at the upper end of 4.1 mmol L^{-1} at pH 7 and 1.7 mmol L^{-1} at pH 6, respectively (cf. Table 1).

At pH 7, an almost symmetric distribution of the three types of oxidation rate occurs (Fig. 3a). The highest rate is obtained by heterogeneous abiotic oxidation with almost $4 \bullet 10^{-8}$ mol L^{-1} s^{-1}. Under these conditions the amount of ferric (oxyhydr)oxide able to adsorb Fe(II) is high and has a maximum at the centre of the biofilm (Fig. S5).

The symmetric pattern reflects the vertical concentration distribution of both Fe(II) and O_2 with Fe(II) diffusing from the lower to the upper end and O_2 from the upper end (Fig. 2). The maximum of the concentration product of the two reactants (Fe(II) and O_2) is also located

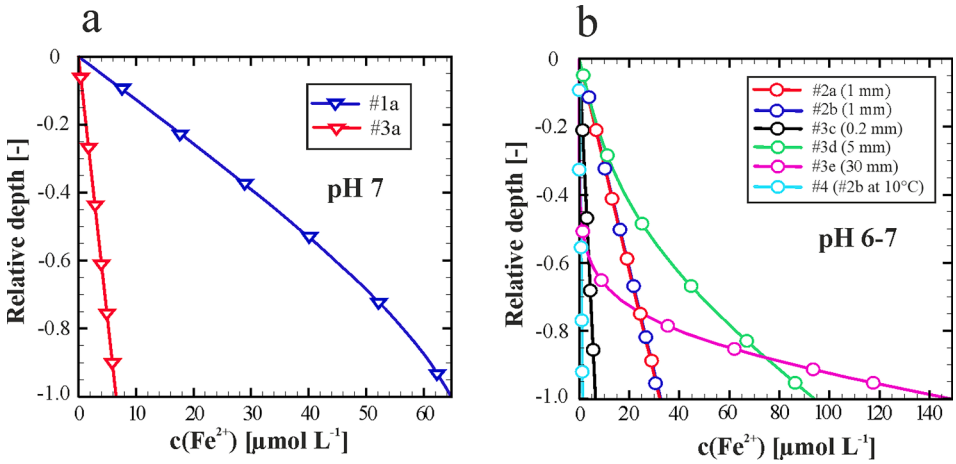

Fig. 2. Concentration gradients of Fe(II) simulated for the various scenario boundary conditions. a) constant pH, film thickness 1 mm (scenario #1a) and 0.2 mm (#3a); b) variable pH and variation of film thicknesses. In order to compare different film ticknesses we have normalized the depth to the filmthick ness (relative depth).

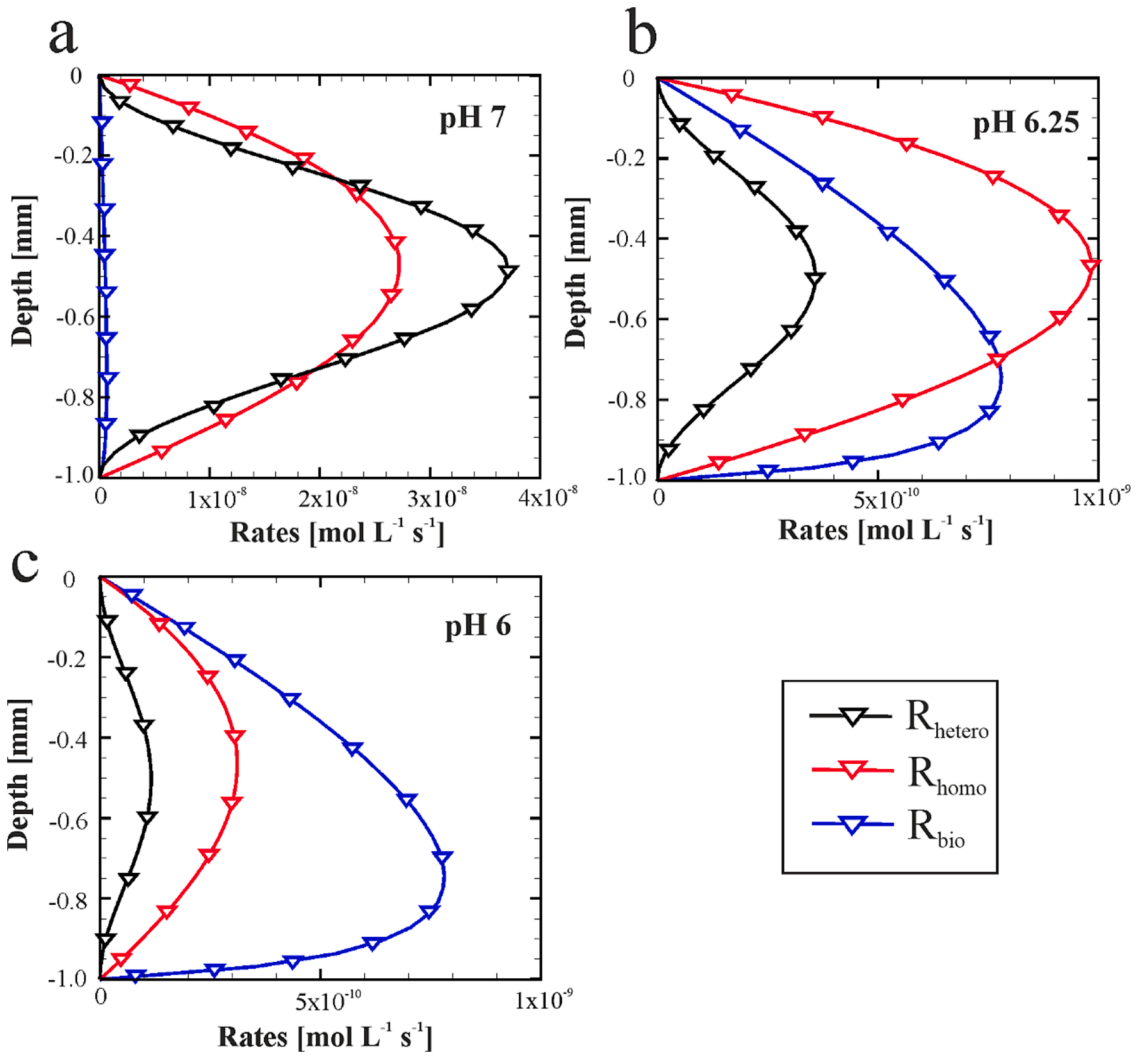

Fig. 3. Scenario #1: Spatial distribution of rates of Fe(II) oxidation rates at a) constant pH 7, b) constant pH 6.25, c) constant pH 6. R_{homo}, R_{hetero}, and R_{bio} refer to homogeneous, heterogeneous and biological oxidation rates, respectively. TIC is 5 mmol L^{-1} at the bottom at both pH values and variable values for the various pH values (cf. Tab, 1). Biofilm thickness is 1 mm.

at the center of the biofilm (Fig. S5).

The rate of biological Fe(II) oxidation achieves a maximum value of $6.7 \bullet 10^{-10}$ mol L^{-1} s^{-1}. This rate is in the range reported by Maisch et al. (2019). They reported biological Fe(II) oxidation rates of between 0.1 and 8 $\times$ 10^{-15} mol Fe(II) $cell^{-1}$ h^{-1}. Using their cell numbers ($3 \bullet 10^6$ cells mL^{-1} on average) one obtains microbial oxidation rates ranging between 1.4 $\times$ 10^{-10} and 8.5 $\times$ 10^{-10} mol L^{-1} s^{-1}. Apparently, the three oxidation processes operate in parallel to a different extent.

At lower pH values (6.25 and 6.0), the distribution pattern for oxidation kinetics considerably changes compared to pH 7 (Figs. 3b and 3c). Abiotic rates of Fe(II) oxidation decrease by 2 orders of magnitude, accompanied by a predominance shift from heterogeneous oxidation at pH 7 to homogeneous oxidation at pH 6.25. At pH 6, biological oxidation is the predominant reaction with rates being a little higher than at pH 7 but again in the range measured by Maisch et al. (2019). The reason for this pH dependent pattern is i) the decrease of adsorption of Fe(II) to ferric (oxyhydr)oxides from pH 7 to pH 6, supressing heterogeneous oxidation and ii) the pH dependence of homogeneous oxidation rate (cf. equation S 1.1).

We have also tested the effect of constant TIC concentrations at both ends of the film, which revealed negligible effects on the overall pattern of the spatial distribution of reaction rates at constant pH values.

3.3. Scenario #2: Effect of pH gradients and alkalinity gradients on spatial distribution of Fe(II) oxidation rates

The situation completely changes once pH gradients were considered within the film layer. In scenario 2, the pH was again 7 at the upper end of the biofilm, while it was 6 at the lower end. Biofilm thickness was constrained to 1 mm again. In this series of scenarios, we have varied the TIC and alkalinity as described in Table 1. Scenario 2a reflects conditions of constant TIC at both ends which implies not only a gradient in pH but also in alkalinity (Fig. S4b). Inversely, in scenario 2b, the alkalinity was kept constant throughout the entire biofilm implying a gradient in TIC. As a consequence, pH gradients vary between the two scenarios (Fig. S4a). At the center of the biofilm, the pH is only 6.25 in scenario 2b (constant alkalinity), but achieves a value of 6.45 in scenario 2a (alkalinity gradient).

As a consequence, the rates also vary between the two scenarios (Fig. 4). Generally, a clear splitting between predominance of abiotic homogeneous Fe(II) oxidation in the upper part of the biofilm and predominance of biological Fe(II) oxidation in the lower part can be observed. However, conditions of higher alkalinity (pH buffer capacity) at the upper end (scenario 2a) amplify homogeneous Fe(II) oxidation rates as compared to conditions where alkalinity is constant throughout the biofilm. Biological oxidation rates are very similar in both scenarios.

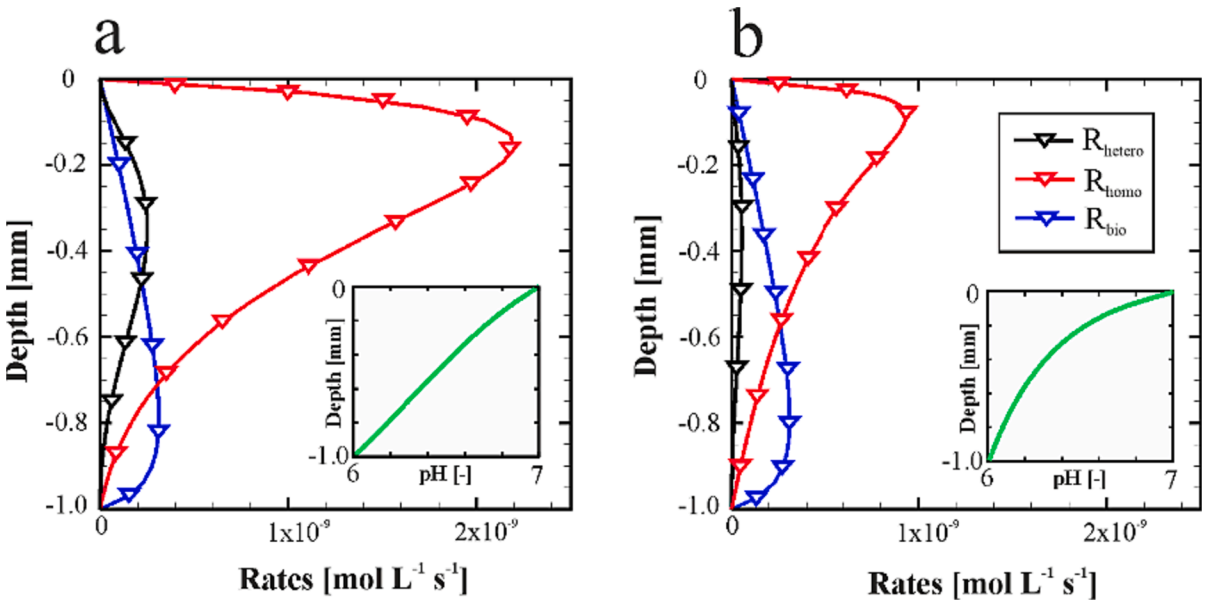

Fig. 4. Scenario 2a and b: Spatial distribution of Fe(II) oxidation rates in a biofilm of 1 mm thickness with pH 7 at the upper end and pH 6 at the lower end of the biofilm. a) Constant TIC = 5 mmol L^{-1} (scenario 2a), b) constant alkalinity = 1.7 mmol L^{-1} (scenario 2b, cf. Table 1 for corresponding alkalinity and TIC concentrations, respectively). The inserts denote the spatial change of pH.

Scenario 2 suggests that processes that establish pH gradients within a biofilm result in distinct zones of predominance of a certain oxidation process, with the shape of the pH gradients affecting the respective rates.

3.4. Scenario #3: Effect of biofilm thickness on spatial distribution of Fe (II) oxidation rates

Biofilm thickness has a major effect on the spatial distribution of Fe (II) oxidation rates. At a biofilm thickness of 0.2 mm and at constant pH values (scenarios as in Table 1), heterogeneous Fe(II) oxidation does not play a role even at pH 7 (Fig. 5a and 5b, note that the black line denoting heterogeneous oxidation is overlapping with the y-axis), due to the low concentration of aqueous Fe(II) and subsequently of adsorbed Fe(II) (Fig. 2). Hence, one reaction pathway predominates over the other: At pH 7, homogeneous oxidation is predominant while at pH 6 it is biological oxidation. Biological oxidation, however, proceeds at a very low rate (maximum rate is 6.3 10^{-11} mol L^{-1} s^{-1}).

Under conditions of a pH gradient (upper end pH 7 and lower end pH 6, TIC and alkalinity as in scenario 2b), an even more pronounced splitting of the zonation can be observed at a biofilm thickness of 0.2 mm (Fig. 5c) when compared to a thickness of 1 mm (Fig. 4b).

In contrast, at a biofilm thickness of 5 mm and 30 mm and despite the pH gradient, heterogeneous oxidation is clearly the dominant pathway (Fig. 6). At a thickness of 5 mm, a stratification of oxidation rates can be observed within the biofilm with a maximum in the abiotic homogeneous oxidation rate right at the upper end of the biofilm, the maximum abiotic heterogeneous oxidation rate ($6 \bullet 10^{-9}$ mol L^{-1} s^{-1}) at 2.5 mm depth, and a very thin layer at the bottom of the biofilm where biological Fe(II) oxidation prevails with a maximum oxidation rate of approx. $0.6 \bullet 10^{-9}$ mol L^{-1} s^{-1}. A similar pattern can be observed at a thickness of 30 mm, however the reactive Fe(II) oxidizing zone is constrained to the lower half of the film due to the complete consumption of Fe(II) at this depth. As discussed in section 3.1, the reduced O_2 flux at larger film thickness leads to an increase of the Fe(II) concentration at the bottom (Fig. 2), that allows for a larger fraction of Fe(II) to adsorb at the mineral surfaces, driving heterogeneous reactions.

3.5. Scenario #4: Effect of temperature on spatial distribution of Fe(II) oxidation rates

All scenarios above were calculated with parameters that either matched room temperature or that were taken as standard values at 25 °C. This temperature is certainly an upper limit for many freshwater systems. We therefore investigated the effect of a temperature matching groundwater conditions, i.e. 10 °C, on the spatial distribution of Fe(II) oxidation rates. The following corrections were made: i) reduction of the diffusion coefficient by a factor of 1.7 following the considerations given in Zhang (2008), ii) reduction of K_s and ν_{max} by a factor of 0.3 which matches a rule of thumb based on Q_{10} values (change of rate per 10 °C temperature difference) discussed in Brezonik (1994), and iii) increase of solubility of dissolved oxygen from 0.27 mmol L^{-1} to 0.37 mmol L^{-1}. The effect of temperature on abiotic oxidation kinetics appears to be minor (Sung and Morgan, 1980) so that no correction was performed. Likewise, acidity constants of carbonic acid were not changed. The simulations were performed based on input parameters from scenario 2b and the results can be directly compared with those displayed in Fig. 4b at the bottom.

As expected, rates at 10 °C are distinctly lower than at 25 °C (Fig. 7). Interestingly, separation between homogeneous oxidation and biological oxidation is even sharper than at 25 °C. The reason for this is related to the distinctly lower diffusion velocity of Fe(II) at this temperature, which leads to a much lower dissolved Fe(II) concentration in the biofilm (Fig. 2). As a consequence, heterogeneous Fe(II) oxidation becomes negligible.

3.6. Spatial distribution of pH values and cells in a biofilm

Fig. 8 shows a confocal laser scanning microscopy-dataset of a biofilm from an iron-rich mine. The biofilm contains Fe(III) (oxyhydr) oxide-encrusted twisted stalks that are characteristic for microaerophilic Fe(II)-oxidizing bacteria (Chan et al., 2009). The biofilm is rich in Fe(II) triggered by intensive Fe cyling. Correlations were found between the channels of the EPS staining lectin-dye conjugate PNA-Alexa Fluor™ 568 and of the Fe(II)-specific fluorescence sensor 2 (Fig. S6). These results demonstrate a complexation of Fe(II) in fractions of the twisted stalks formed by microaerophilic Fe(II)-oxidizing bacteria amongst

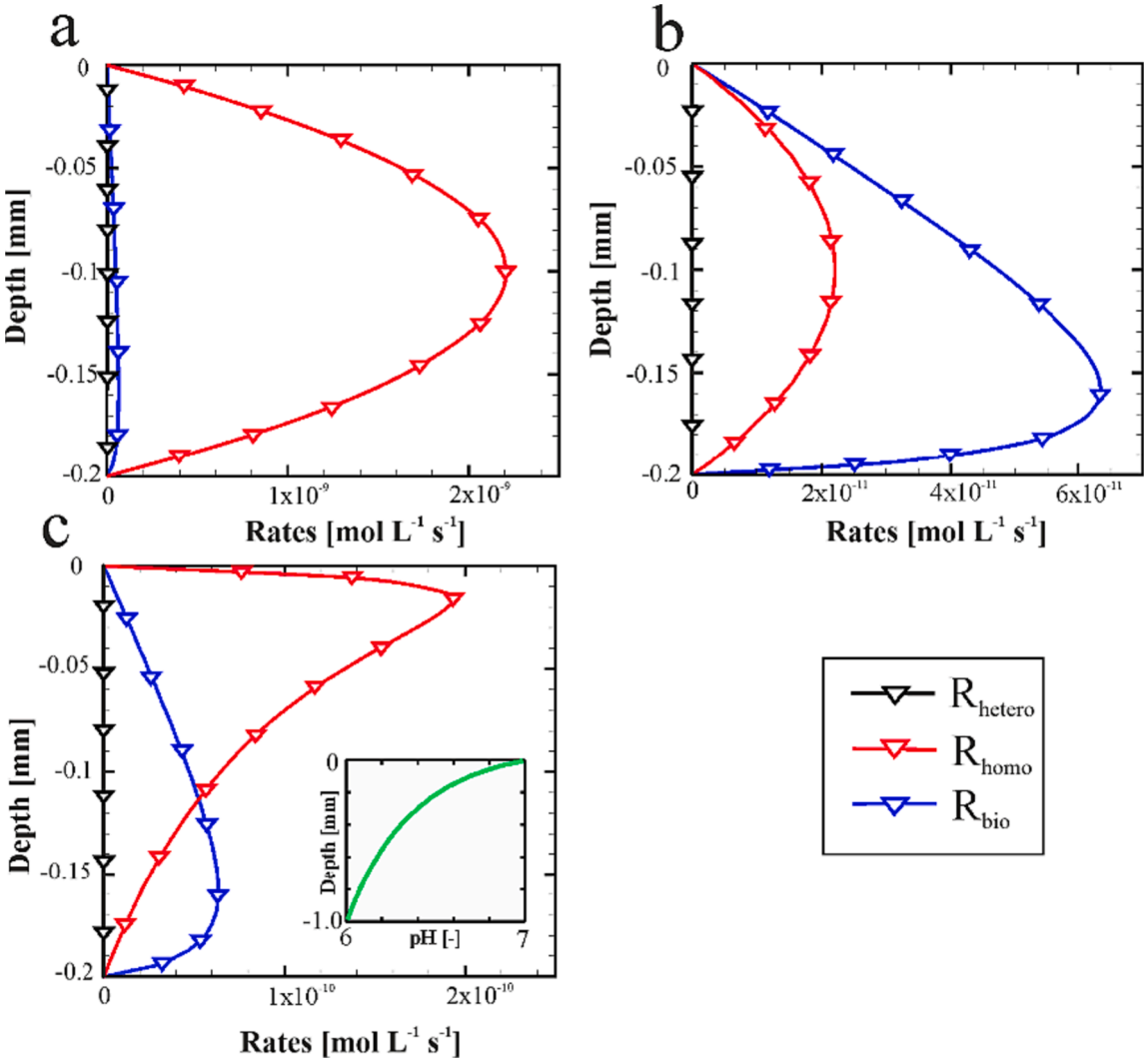

Fig. 5. Scenario 3a-c: Spatial distribution of Fe(II) oxidation rates at a biofilm thickness of **0.2 mm** a) at uniform pH 7, b) at uniform pH 6; TIC is 5 mmol L^{-1} at the bottom and 4.1 mmol L^{-1} at the upper end of the biofilm as in scenario 1a (Table 1), c) pH 7 at the upper end and pH 6 at the lower end of the biofilm. TIC and alkalinity as in scenario 2b (Table 1).

other microbial EPS structures.

A three-dimensional biofilm layer (117 x 117 x 39 micrometer) was analyzed in its original sample water, 20 min after staining with the ratiometric pH-sensitive fluorescence dye SNARF-4f. A frequency analysis of the voxels revealed a mean pH of ~ 6.9. Microbial cells made up approximately 1 vol% of the biofilm. A subfraction of the cells (cells illustrated in red in Fig. 8) showed acidified surroundings with pH < 6.7 that made up in total 10 vol%, and a pH as low as pH 6.0 in particular acidic spots.

4. Discussion

4.1. Kinetic controls on spatial distribution of Fe(II) oxidation processes

The simulations revealed a complex interplay of factors affecting the spatial distribution of the three Fe(II) oxidation processes as well as their rates. Kinetically controlled geochemical processes establish the zones in which biological Fe(II) oxidation is the predominant and under some conditions the exclusive Fe(II) oxidation process. These niches are found at low pH (i.e. close to 6), where the other oxidation processes slow down due their pH dependent rate laws. These niches are very distinct under conditions of a short diffusion path (a thin 0.2 mm biofilm) or at low temperatures (10 °C) when O_2 concentrations are higher.

Alkalinity plays a major role in affecting microniches formation by control of the spatial pH distribution. Under conditions of a pH gradient at a constant alkalinity of 1.7 mmol L^{-1} (scenario#2b, Fig. 4), predominance of biological Fe(II) oxidation is achieved at a distinctly lower depth (z = 0.55 mm) as compared to conditions where the alkalinity is generally higher and reaches the value of 1.7 mmol L^{-1} only at the lower end of the biofilm (scenario#2a, z = 0.7 mm). Hence, alkalinity, i.e. the buffer capacity against formation of acidity following hydrolysis reactions of Fe^{3+} (reaction S 1.9) of a biofilm, will have a paramount influence on the formation of microniches favourable for Fe(II)-oxidizing bacteria. In the environment, alkalinity can be highly variable. The seepage water on which the biofilm sampled for this study grew had an alkalinity of 6.3 mmol L^{-1}. In coastal sediments, alkalinity ranges between 2 and 5 mmol/L in sulfide-oxidizing sediments (Rao et al., 2016) and can be as low as 0.2 mmol L^{-1} in epilimnetic lake sediments (Schiff and Anderson, 1986).

The importance of pH for the occurrence of biological Fe(II) oxidation is underpinned by the observation of pH values distinctly lower than 6.7 in a biofilm obviously rich in Fe(II). We interpret these spots as indicative of active Fe(II)-oxidizing bacteria. The distances between spots of differing pH values are rather short (~10 um) and suggest an active contribution of cells to the pH drop in a high-alkalinity environment. If we consider only the acidity production stemming from the

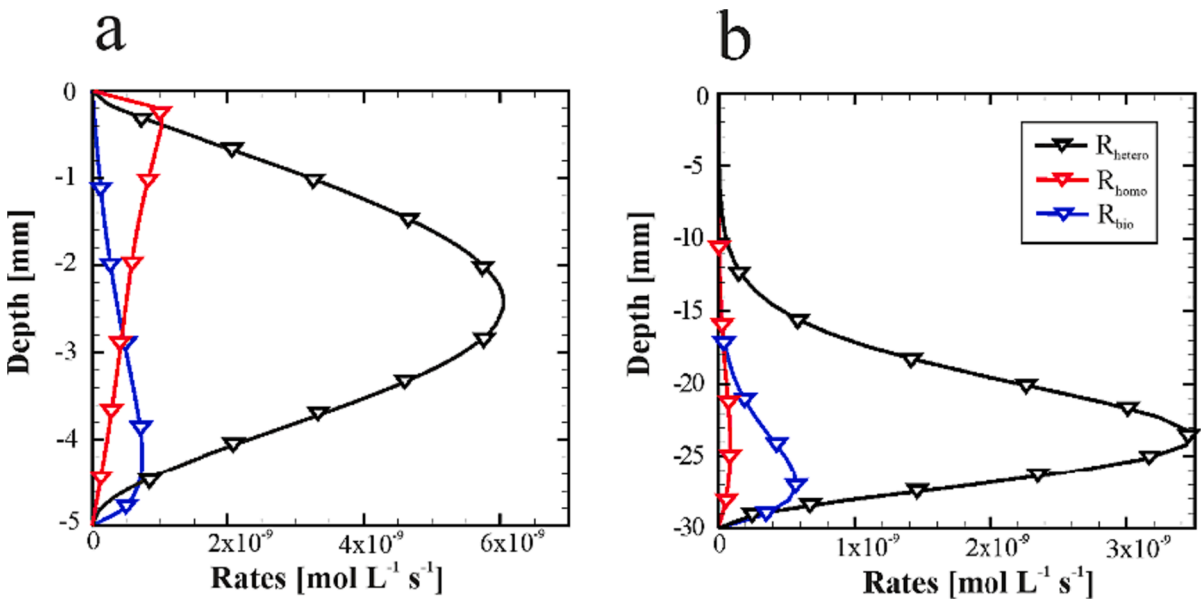

Fig. 6. Scenario 3d-e: a) Spatial distribution of Fe(II) oxidation rates in a biofilm thickness with pH 7 at the upper end and pH 6 at the lower end of the biofilm. TIC and alkalinity as in scenario 2b (Table 1), a) film thickness 5 mm, b) film thickness 30 mm.

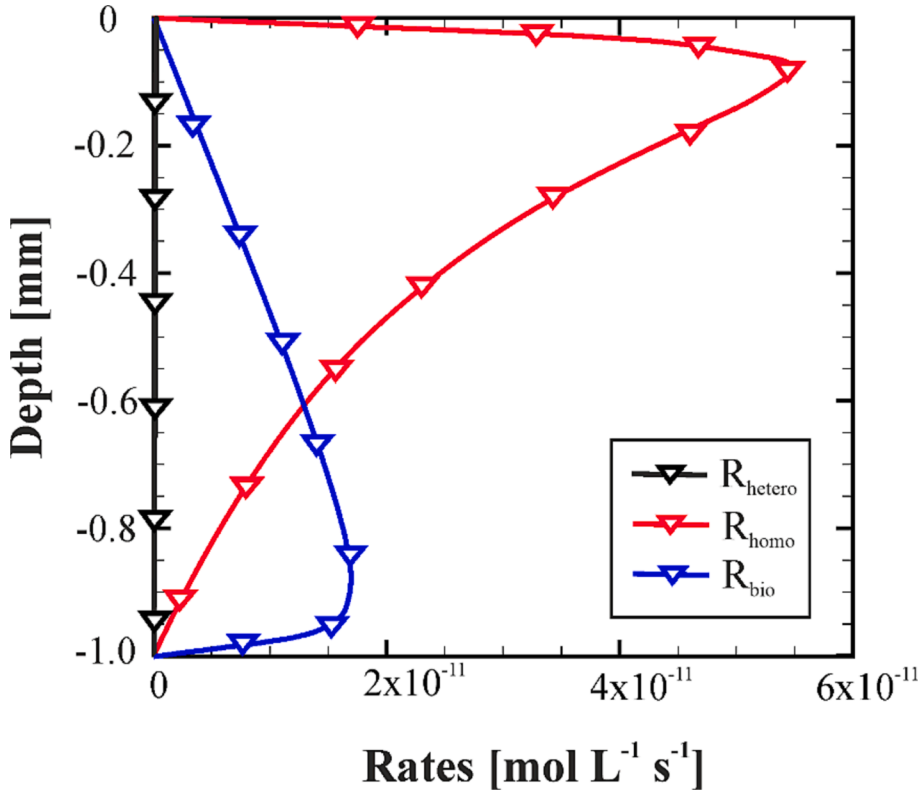

Fig. 7. Scenario 4: Spatial distribution of Fe(II) oxidation rates in a biofilm at T = 10 °C under the same boundary conditions as in scenario 2b.

formation of ferric (oxyhydr)oxides during the reaction (~4 • 10^{-5} mol L^{-1}), this would not be sufficient to allow for a substantial pH drop at the alkalinity in the model systems. Fe(II) oxidation seems to be reaction-limited at these distances. A Damköhler analysis of the oxidation reactions reveals that Damköhler numbers were distinctly less than 1 (cf. SI section 5 for derivation) at film thicknesses ≤ 1 mm indicating that pH gradients as observed in Fig. 8 are clearly reaction-controlled (Oldham et al., 2019) and maintained by active contribution of the cells. At the same time, the observed heterogeneity of pH within the analyzed biofilm indicates that Fe(II)-oxidizing microorganisms are actively influencing their microenvironment towards their metabolic optimum.

It appears that conditions of predominance of biotic Fe(II) oxidation can be predicted based on an analysis of characteristic reaction time scales for abiotic and biological oxidation. To these ends, equations (S 1.1) and (S 1.2) were converted into pseudo-first order reactions:

$$\frac{dc(Fe^{2+})}{dt} = -k_{pseudo} \bullet c(Fe^{2+})$$

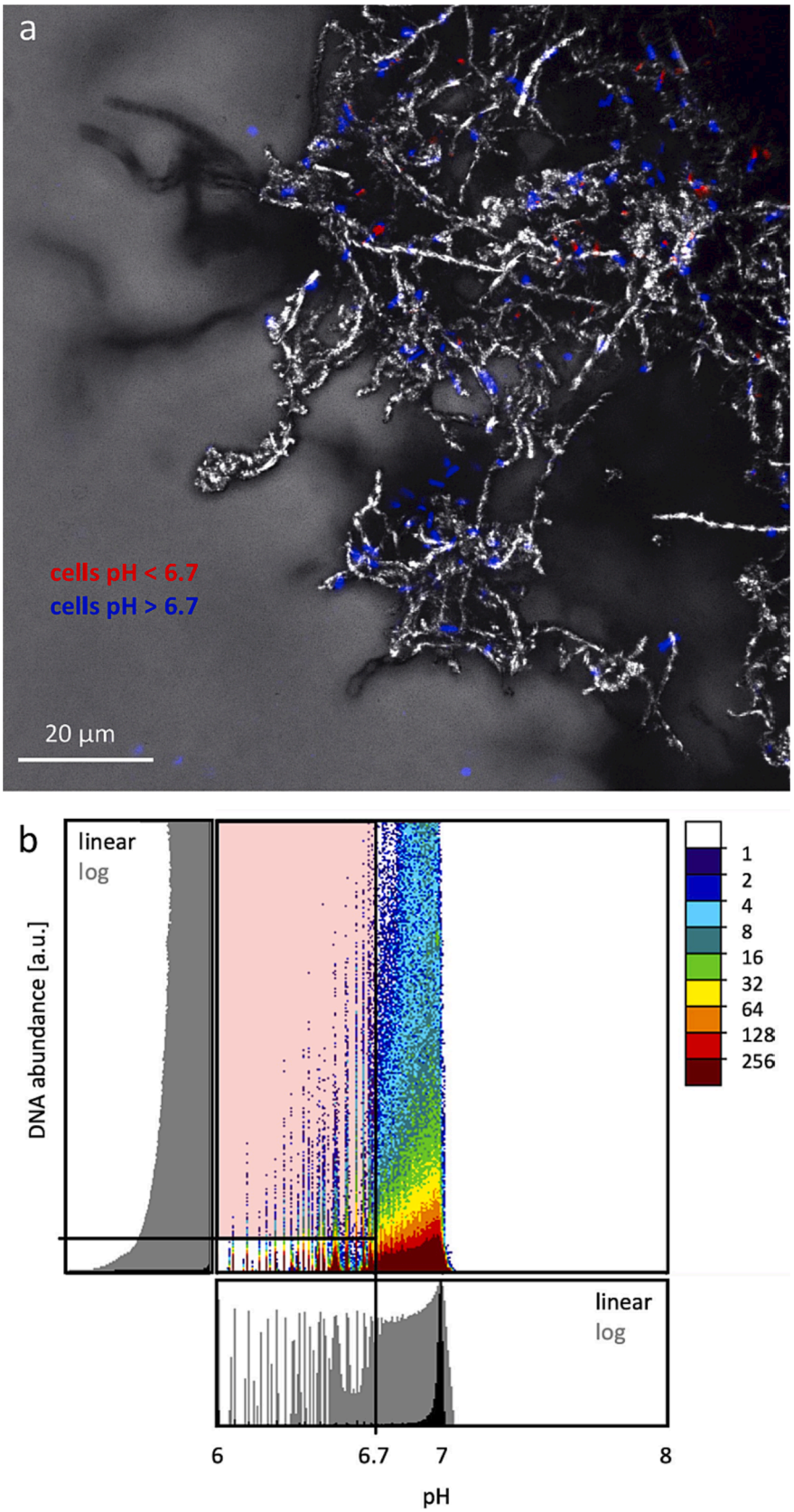

(caption on next page)

Fig. 8. A) Maximum intensity projection of a 3D CLSM dataset of an Fe(II)-oxidizing biofilm that was stained with the DNA stain Syto 40 and the ratiometric pH sensitive fluorescence stain SNARF-4f. The projection is superimposed on the minimum intensity projection of the non-confocal transmission channel visualizing the overall structure of the biofilm. Cells with an acidic microenvironment of pH < 6.7 were identified at conditions of a bulk volume of pH = 6.9 by correlative image analysis and are illustrated in red, whereas all other cells are shown in blue. The reflection signals in white are mainly caused by the Fe(III) (oxyhydr)oxide encrusted twisted stalks produced by the bacteria. b) Scatterplot for the entire measured volume of the signal of the DNA fluorescent stain Syto 40 vs. pH, which was calculated based on ratiometric fluorescent images of the pH-sensitive SNARF 4f dye. The light red region marked in the scatterplot indicates the values used for backmapping of the acidic cells (cells illustrated red in Fig. 8a). In the respective histograms (both linear and logarithmic) of the cell mapping for DNA (left, Syto40 channel) and pH (bottom, pH-range 6–8) the used threshold values are marked as black lines.

with k_{pseudo} depending on the oxygen concentration and, in the case of both homogeneous and heterogeneous oxidation reactions, also on pH at each depth (cf. equations S 5.1 – S 5.3). Characteristic reaction time scales are then:

$$t_{char,homo} = 1/k_{pseudo,homo}$$
$$t_{char,hetero} = 1/k_{pseudo,hetero}$$
$$t_{char,biotic} = 1/k_{pseudo,biotic}$$

The ratios between these time scales:

$$\theta_{homo} = t_{char,homo}/t_{char,biotic}$$
$$\theta_{hetero} = t_{char,hetero}/t_{char,biotic}$$

can be used to analyze the conditions with regard to the predominance of a certain process. If $\theta > 1$ (i.e. $\log \theta > 0$, Fig. 9), biological Fe(II) oxidation is dominant and vice versa. Fig. 9 plots the logarithm of θ as a function of relative biofilm thickness.

This analysis clearly illustrates that there is a kinetic control on oxidation rates with a predominance area for biological oxidation in the right side of Fig. 9. It predicts predominance of abiotic oxidation for conditions as in scenario #1a, i.e. constant pH 7. Heterogeneous Fe(II) oxidation is kinetically favoured across most of the film thickness, while inversely, at conditions of constant pH 6, biotic oxidation is clearly favoured. However, at conditions of pH gradients (scenarios #2b and #3c), the situation appears to be more complex. Conditions change from predominance of homogeneous abiotic oxidation to biotic oxidation at a relative depth of 0.4, which in these scenarios implies that biological oxidation is favoured at pH values below 6.3 and dissolved oxygen concentrations below 150 μmol L^{-1}.

Interestingly, in these scenarios, heterogeneous oxidation seems not to be competitive under any conditions. Heterogeneous oxidation requires a certain surface coverage with Fe(II) which also depends on the total amount of sorption sites, which again is a function of the total amount of ferric (oxyhydr)oxides generated. At a low film thickness (0.2 mm), the concentration of Fe(II) becomes very low following the increased O_2 flux (cf. section 3.1, Fig. 2). Under these conditions, the concentration of precipitated $Fe(III)_{solid}$ (and along with that the concentration of adsorbed Fe(II)) also becomes very low even at pH 7 (scenario #3a, $c(>Fe(OH)_{tot} < 10^{-7}$ mol L^{-1}). In contrast, if the O_2 flux

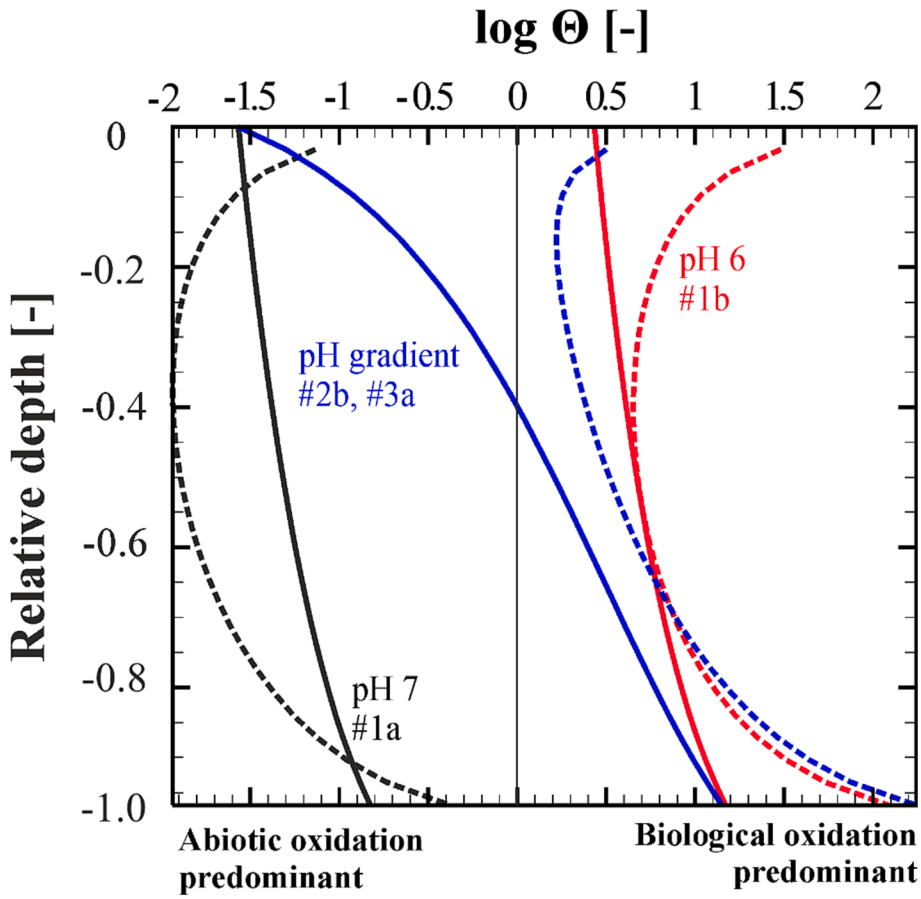

Fig. 9. Spatial distribution of the logarithmic ratio between characteristic time scales θ in a biofilm calculated based on scenarios discussed above. Dashed lines refer to θ_{hetero} and straight lines to θ_{homo}. Note that the spatial distribution of log θ calculated with boundary conditions as in scenario 2b is the same for a biofilm thickness of 1 and 0.2 mm.

becomes lower because the film thickness is larger (5 mm, scenario #3d; 30 mm, scenario #3e Fig. 2), heterogeneous oxidation becomes the predominant Fe(II) oxidation process ($c(Fe(III)_{solid}) > 10^{-6}$ mol L^{-1}).

Overall, this analysis demonstrates that the spatial distribution of oxidation processes is an intricate interaction between chemical boundary conditions driving the reaction kinetics (pH, alkalinity) and physical boundary conditions driving the supply rates of the reactants (film thickness).

4.2. Energetics of biological oxidation of Fe(II)

The computed biological oxidation rates are generally quite low, even though they can outcompete abiotic rates in some cases. Minimum rates were $< 10^{-12}$ mol L^{1-} s^{-1} and thus distinctly lower than those observed in experimental studies (Maisch et al., 2019). We therefore tested whether these low rates allow for sufficient energy gain beyond cell maintenance. To this end, the calculated biological rates R_{bio} were corrected using a thermodynamic factor F_T proposed by (Bethke, 2008) to account for the availability of energy:

$$R'_{bio} = R_{bio} F_t$$

The factor F_T accounts for the free energy of a redox reaction and the energy conserved by respiration:

$$F_T = 1 - \left(\frac{Q}{K}\right)^{\frac{1}{\chi}} \bullet \exp\left(\frac{\Delta G_{ATP}}{\chi RT}\right) \quad (1)$$

Q: Quotient of the activities of the reactants of the energy delivering redox reaction, which is in this case the oxidation of Fe(II) to ferrihydrite by O_2 (Emerson et al., 2010; Maisch et al., 2019),

$$Fe(II) + ¼\ O_2 + 1.5\ H_2O \rightarrow FeOOH + 2H^+$$

$$Q = \frac{a(H^+)^2}{a(Fe^{2+})a(O_2)^{0.25}}$$

K: equilibrium constant for the reaction which can be calculated from ΔG°_{redox} (-29.3 kJ mol^{-1}) to be $10^{5.14}$ (cf. SI section 7 for derivations)

χ: average stoichiometric number denoting the number of protons transferred per electron in the rate limiting step. Following the proposed proton transfer chain for microaerophilic oxidation of Fe(II) proposed in Becker et al. (2021) predicting 1 proton transfer per electron and the considerations made in Jin and Bethke (2003), the value for χ was set to 1.

ΔG_{ATP}: energy conserved by respiration, ΔG_{ATP} was calculated to be 60 kJ mol^{-1} (cf. SI section 7)

Under suitable conditions, i.e. sufficient substrate availability, F_T in Eq. (1) is equal to 1 and the energy available is much larger than the amount of energy conserved for maintenance (Jin and Bethke, 2005). If the energy available approaches the maintenance energy, F_T assumes a value less than 1 and becomes zero if respiration comes to cessation.

In all scenarios F_t values were lower than 1. Lowest biological oxidation rates were found in simulations with a film thickness of 0.2 mm (scenarios #3b and #3c), presumably due to the low Fe(II) concentration under these conditions. In these scenarios, F_t values were negative in the upper third of the film at very low Fe(II) activities ($\leq$2 µmol L^{-1}) despite a dissolved oxygen concentration $\geq$ 160 µmol/L. indicating that under these conditions microaerophilic Fe(II) oxidation would energetically not be possible. F_t values stayed less than 0.4 below a depth of 0.08 mm. As a consequence, corrected biological rates are much less than those simulated (Fig. S7).

The cause for the low Fe(II) concentrations in these scenarios is the balance between the O_2 flux as being controlled by the film thickness and the Fe(II) flux, which is a function of microbial Fe(III) reduction rate in the reducing layer underneath the anoxic–oxic interface. Hence, our simulations imply that biological oxidation of Fe(II) under these boundary conditions operates right at the thermodynamic threshold and is further constrained by the supply rates of reactants.

Exergonicity of the redox reaction at circumneutral pH also depends on the extent to which the activity of the primary reaction product Fe^{3+} is lowered. In contrast to more crystalline minerals such as goethite, ferrihydrite has a higher solubility and therefore, also ΔG°_{redox} with ferrihydrite as final product (-29.3 kJ mol^{-1}) is distinctly higher than that of goethite (-44.3 kJ mol^{-1}). Ferrihydrite, however, was identified as the most likely reaction product in the experiments performed by (Maisch et al., 2019) and it is reported to be the common reaction product of biological Fe(II) oxidation (Emerson et al., 2010). It is interesting to note that the standard enthalpy of formation ΔG_f° of ferrihydrite is very sensitive to the thermodynamic factor F_T. ΔG_f° values for specimen prepared at different synthesis time scales (Majzlan et al., 2004) were critically compiled by Hiemstra (2015). Two-line ferrihydrite aged for 2 h has a value of only −472.8 kJ mol^{-1} compared to the 24 h aged specimen used in our analysis of F_t with $\Delta G_f^\circ = -475.6$ kJ mol^{-1}. The value ΔG°_{redox} for the redox reaction than increases to −26.9 kJ mol^{-1} which leads to negative F_t values throughout the entire film thickness in scenarios #3b and #3c.

It may therefore be speculated that other controls on Fe^{3+} activities may contribute to a higher energy yield. When studying organic stalk formation, Chan et al. (2011) have demonstrated that Fe(III)-polysaccharide complexes are excreted from a cell with Fe(III)-precipitates (ferrihydrite) forming over time. This observation suggests that Fe(III)-complexes were exudated and Fe(III)-precipitates may not be at equilibrium. Hence, if Fe(III)-complexes are very strong they may shift the equilibrium by lowering Fe^{3+} concentrations to values that in turn decrease the value of ΔG°_{redox} in the redox reaction.

$$Fe(II) + 0.25\ O_2 + L^- + H^+ \rightarrow FeL^{2+} + 0.5\ H_2O$$

below the −29.3 kJ mol^{-1} of the reaction with ferrihydrite as a reaction product (equation S 6.1), with ferrihydrite being a kinetically-controlled reaction product independent of the redox reaction.

5. Conclusions and Implications

This simulation experiment has demonstrated that biological oxidation of Fe(II) occurs in all studied scenarios, albeit at partly very low rates and in most cases close to the thermodynamic threshold. The spatial distribution of the various Fe(II)-oxidizing processes is strongly controlled by pH and alkalinity. The relative contribution of each oxidation pathway depends on the balance between the Fe(II) flux and the oxygen flux. In our simulations, at constant Fe(II) flux, heterogenous reaction was predominant at low O_2 fluxes that were controlled by the film thickness. Our simulations allow to constrain the niche for microaerophilic Fe(II)-oxidizing bacteria. They additionally raise the question as to whether microbial strategies exist to enhance their competitiveness and for which our study clearly indicates a variety of strategic options.

It appeared that low pH values are kinetically favouring microbial Fe(II) oxidation over abiotic processes. Hence, exudation of acids/acidic functional groups such as carboxylic groups in the extracellular polymeric substances may lead to transient acidic spots as being visualized in Fig. 8. Alternatively, Fe(II)-oxidizing bacteria may benefit from the decrease in abiotic oxidation rates upon complexation within the biofilm structure (as shown in Fig. S6) or other organic Fe(II)-complexing agents. Several natural organic compounds have been demonstrated to increase half-lives of Fe(II) relative to pure (sea water) solutions (Rose and Waite, 2002; Rose and Waite, 2003), depending on their redox potential. Indeed, addition of humic acid extracts stimulated biological Fe(II) oxidation in peatlands (Hädrich et al., 2019) or for

photautotrophic Fe(II)-oxidizing bacteria (Peng et al., 2019). Abiotic Fe (II) oxidation was slow or negligible in the presence of naturally occurring organics, which would allow microaerophilic Fe(II) oxidation to be a prominent mechanism at low O_2 concentrations (Zhou et al., 2021). These authors discussed the various mechanisms through which organic ligands can interfere in the competition between abiotic and biotic Fe(II) oxidation and therefore, production of substances inhibiting abiotic Fe(II) oxidation but allowing for biotic oxidation might be an obvious strategy. In a similar way, heterogeneous oxidation rates may also be affected upon production of substances that decrease the adsorption capacities of ferric (oxyhydr)oxides or lead to passivation of their surfaces. In this context, extracellular polymeric substances (EPS) may have a profound effect on both homogeneous and heterogeneous Fe (II) oxidation rates, with biogenic ferric (oxyhydr)oxides being less susceptible to heterogeneous oxidation.

In a broader sense, the film layer, which we have treated as just a diffusive barrier between Fe(III) reducing bacteria and the surrounding water body, reflects a macroscopic model of the interface between Fe (III) reducing and O_2 producing environments, such as benthic algae or cyanobacteria that provides ingredients enhancing competitiveness for Fe(II) oxidizing bacteria. The heterogeneity of pH values observed in such an environment (Fig. 8) demonstrates that Fe(II)-oxidizing microorganisms may be able to outcompete abiotic reactions even under macroscopic conditions that are not ideal, and growth of microaerophilic Fe(II)-oxidizing might not be strictly limited to the conditions suggested by the simulations. Our simulations have identified the kinetic constraints that Fe(II)-oxidizing microorganisms need to overcome to enhance their competitiveness against abiotic reactions and that should guide future research on the role of biological Fe(II)-oxidation in the environment.

Data availability

Data are available through Zenodo at https://doi.org/10.5281/zenodo.8010462.

Declaration of Competing Interest

The authors declare that they have no known competing financial interests or personal relationships that could have appeared to influence the work reported in this paper.

Acknowledgements

This research has evolved from fruitful discussions at the Iron Biogeochemistry Workshop 2018 in Lech. We acknowledge the valuable input from Clara Chan provided during an ACS conference. The authors are grateful for financial support obtained through the project "*AquaKlif - Influence of multiple climate-change stressors on stream ecosystems*" from the *Bavarian Climate Research Network bayklif*. AK acknowledges infrastructural support by the Deutsche Forschungsgemeinschaft (DFG, German Research Foundation) under Germany's Excellence Strategy, cluster of Excellence EXC2124, project ID 390838134. MO acknowledges the support by the DFG (Heisenberg grant OB 362/7-1 and project OB 362/4-1) We further appreciate the very constructive comments from four anonymous reviewers.

Appendix A. Supplementary material

The following are the Supplementary data to this article:

Details of Modeling approach, Derivation of kinetic coefficients, additional simulation results, Derivation of Damköhler numbers, additional data on confocal laser scanning microscopy, derivation of thermodynamic factor FT, additional Figures.

Supplementary material to this article can be found online at https://doi.org/10.1016/j.gca.2023.11.006.

References

Becker, S., Enright, A., Kappler, A., 2021. Living on Iron. In: Kroneck, P.M.H., Sosa Torres, M.E. (Eds.), Metals, Microbes, and Minerals - the Biogeochemical Side of Life. De Gruyter, Berlin.

Bethke, C.M., 2008. Geochemical and Biogeochemical Reaction Modelling. Cambridge University Press.

Brezonik, P.L., 1994. Chemical Kinetics and Process Dynamics in Aquatic Systems. Lewis Publkishers.

Cai, W.J., Reimers, C.E., Shaw, T., 1995. Microelectrode studies of organcii carbon degradation and calcite dissolution at a California Continental rise site. Geochim. Cosmochim. Acta 59 (3), 497–512.

Chan, C.S., Fakra, S.C., Edwards, D.C., Emerson, D., Banfield, J.F., 2009. Iron oxyhydroxide mineralization on microbial extracellular polysaccharides. Geochim. Cosmochim. Acta 73 (13), 3807–3818.

Chan, C.S., Fakra, S.C., Emerson, D., Fleming, E.J., Edwards, K.J., 2011. Lithotrophic iron-oxidizing bacteria produce organic stalks to control mineral growth: implications for biosignature formation. ISME J. 5 (4), 717–727.

Chan, C.S., Emerson, D., Luther, G.W., 2016. The role of microaerophilic Fe-oxidizing micro-organisms in producing banded iron formations. Geobiol. 14 (5), 509–528.

Chiu, B.K., Kato, S., McAllister, S.M., Field, E.K., Chan, C.S., 2017. Novel Pelagic Iron-Oxidizing Zetaproteobacteria from the Chesapeake Bay Oxic-Anoxic Transition Zone. Front. Microbiol. 8, 1280.

Dixit, S., Hering, J.G., 2006. Sorption of Fe(II) and As(III) on goethite in single- and dual-sorbate systems. Chem. Geol. 228 (1–3), 6–15.

Druschel, G.K., Emerson, D., Sutka, R., Suchecki, P., Luther, G.W., 2008. Low-oxygen and chemical kinetic constraints on the geochemical niche of neutrophilic iron(II) oxidizing microorganisms. Geochim. Cosmochim. Acta 72 (14), 3358–3370.

Ehrlich, H.L., Ingledew, W.J., Salerno, J.C., 1991. Iron- and manganese-oxidizing bacteria, in: Shively, J.M. (Ed.), Variations in autotrophic life. Acad. Pr, London, pp. 147–170.

Emerson, D., 2012. Biogeochemistry and microbiology of microaerobic Fe(II) oxidation. Biochem. Soc. Trans. 40 (6), 1211–1216.

Emerson, D., Fleming, E.J., McBeth, J.M., 2010. Iron-oxidizing bacteria: an environmental and genomic perspective. Annu. Rev. Microbiol. 64, 561–583.

Emerson, D., Moyer, C., 1997. Isolation and characterization of novel iron-oxidizing bacteria that grow at circumneutral pH. Appl. Environ. Microbiol. 63 (12), 4784–4792.

Emerson, D., Weiss, J.V., 2004. Bacterial Iron Oxidation in Circumneutral Freshwater Habitats: Findings from the Field and the Laboratory. Geomicrobiol. J. 21 (6), 405–414.

Hädrich, A., Taillefert, M., Akob, D.M., Cooper, R.E., Litzba, U., Wagner, F.E., Nietzsche, S., Ciobota, V., Rösch, P., Popp, J., Küsel, K., 2019. Microbial Fe(II) oxidation by *Sideroxydans lithotrophicus* ES-1 in the presence of Schlöppnerbrunnen fen-derived humic acids. FEMS Microbiol. Ecol. 95 (4).

Hao, L., Guo, Y., Byrne, J.M., Zeitvogel, F., Schmid, G., Ingino, P., Li, J., Neu, T.R., Swanner, E.D., Kappler, A., Obst, M., 2016. Binding of heavy metal ions in aggregates of microbial cells, EPS and biogenic iron minerals measured in-situ using metal- and glycoconjugates-specific fluorophores. Geochim. Cosmochim. Acta 180, 66–96.

Hiemstra, T., 2015. Formation, stability, and solubility of metal oxide nanoparticles: Surface entropy, enthalpy, and free energy of ferrihydrite. Geochim. Cosmochim. Acta 158, 179–198.

Jin, Q., Bethke, C.M., 2003. A new rate law describing microbial respiration. Applied and Environ. Microbiol. 69 (4), 2340–2348.

Jin, Q., Bethke, C.M., 2005. Predicting the rate of microbial respiration in geochemical environments. Geochim. Cosmochim. Acta 69 (5), 1133–1143.

Kappler, A., Benz, M., Schink, B., Brune, A., 2004. Electron shuttling via humic acids in microbial iron(III) reduction in a freshwater sediment. FEMS Microbiol. Ecol. 47, 85–92.

Kappler, A., Bryce, C., Mansor, M., Lueder, U., Byrne, J.M., Swanner, E.D., 2021. An evolving view on biogeochemical cycling of iron. Nat. Rev. Microbiol. 19 (6), 360–374.

Kühl, M., Jørgensen, B.B., 1992. Microsensor measurements of sulfate reduction and sulfide oxidation in compact microbial communities of aerobic biofilms. Appl. Environ. Microbiol. 58 (4), 1164–1174.

Lueder, U., Druschel, G., Emerson, D., Kappler, A., Schmidt, C., 2018. Quantitative analysis of O2 and Fe2+ profiles in gradient tubes for cultivation of microaerophilic Iron(II)-oxidizing bacteria. FEMS Microbiol. Ecol. 94 (2).

Maisch, M., Lueder, U., Laufer, K., Scholze, C., Kappler, A., Schmidt, C., 2019. Contribution of Microaerophilic Iron(II)-Oxidizers to Iron(III) Mineral Formation. Environ. Sci. Technol. 53 (14), 8197–8204.

Majzlan, J., Navrotsky, A., Schwertmann, U., 2004. Thermodynamics of iron oxides: Part III: Enthalpies of formation and stability of ferrihydrite (~Fe(OH)3 schwertmannite (~FeO(OH)3/4(SO4)1/8), and e-Fe2O3. Geochim. Cosmochim. Acta 5 (5), 1049–1060.

Neubauer, S.C., Emerson, D., Megonigal, J.P., 2002. Life at the energetic edge: kinetics of circumneutral iron oxidation by lithotrophic iron-oxidizing bacteria isolated from the wetland-plant rhizosphere. Appl. Environ. Microbiol. 68 (8), 3988–3995.

Oldham, C., Beer, J., Blodau, C., Fleckenstein, J., Jones, L., Neumann, C., Peiffer, S., 2019. Controls on iron(II) fluxes into waterways impacted by acid mine drainage: A Damköhler analysis of groundwater seepage and iron kinetics. Water Res. 153, 11–20.

Peiffer, S., Kappler, A., Haderlein, S.B., Schmidt, C., Byrne, J.M., Kleindienst, S., Vogt, C., Richnow, H.H., Obst, M., Angenent, L.T., Bryce, C., McCammon, C., Planer-

Friedrich, B., 2021. A biogeochemical–hydrological framework for the role of redox-active compounds in aquatic systems. Nat. Geosci. 14 (5), 264–272.
Peine, A., Tritschler, A., Küsel, K., Peiffer, S., 2000. Electron flow in an iron-rich acidic sediment-evidence for an acidity-driven iron cycle. Limnol. Oceanogr. 45 (5), 1077–1087.
Peng, C., Bryce, C., Sundman, A., Borch, T., Kappler, A., 2019. Organic Matter Complexation Promotes Fe(II) Oxidation by the Photoautotrophic Fe(II)-Oxidizer *Rhodopseudomonas palustris* TIE-1. ACS Earth Space Chem 3 (4), 531–536.
Rao, A.M., Malkin, S.Y., Hidalgo-Martinez, S., Meysman, F.J., 2016. The impact of electrogenic sulfide oxidation on elemental cycling and solute fluxes in coastal sediment. Geochim. Cosmochim. Acta 172, 265–286.
Reyes, C., Dellwig, O., Dähnke, K., Gehre, M., Noriega-Ortega, B.E., Böttcher, M.E., Meister, P., Friedrich, M.W., 2016. Bacterial communities potentially involved in iron-cycling in Baltic Sea and North Sea sediments revealed by pyrosequencing. FEMS Microbiol. Ecol. 92 (4), fiw054.
Roden, E.E., Sobolev, D., Glazer, B., Luther, G.W., 2004. Potential for Microscale Bacterial Fe Redox Cycling at the Aerobic-Anaerobic Interface. Geomicrobiol. J. 21 (6), 379–391.
Rose, A.L., Waite, T.D., 2002. Kinetic model for Fe(II) oxidation in seawater in the absence and presence of natural organic matter. Environ. Sci. Technol. 36 (3), 433–445.
Rose, A.L., Waite, D.T., 2003. Effect of dissolved natural organic matter on the kinetics of ferrous iron oxygenation in seawater. Environ. Sci. Technol. 37 (21), 4877–4886.
Rubin-Blum, M., Antler, G., Tsadok, R., Shemesh, E., Austin, J.A., Coleman, D.F., Goodman-Tchernov, B.N., Ben-Avraham, Z., Tchernov, D., 2014. First evidence for the presence of iron oxidizing zetaproteobacteria at the Levantine continental margins. PLoS ONE 9 (3), e91456.
Schiff, S.L., Anderson, R.F., 1986. Alkalinity production in epilimnetic sediments: Acidic and non-acidic lakes. Water Air Soil Pollut. 31 (3–4), 941–948.
Schindelin, J., Arganda-Carreras, I., Frise, E., Kaynig, V., Longair, M., Pietzsch, T., Preibisch, S., Rueden, C., Saalfeld, S., Schmid, B., Tinevez, J.-Y., White, D.J., Hartenstein, V., Eliceiri, K., Tomancak, P., Cardona, A., 2012. Fiji: an open-source platform for biological-image analysis. Nat. Methods 9 (7), 676–682.
Schmidt, C., Behrens, S., Kappler, A., 2010. Ecosystem functioning from a geomicrobiological perspective – a conceptual framework for biogeochemical iron cycling. Environ. Chem. 7 (5), 399.
Sobolev, D., Roden, E.E., 2001. Suboxic deposition of ferric iron by bacteria in opposing gradients of Fe(II) and oxygen at circumneutral pH. Appl. Environ. Microbiol. 67 (3), 1328–1334.
Stumm, W., Morgan, J.J., 1996. Aquatic Chemistry. Wiley, 1022 pp.
Sung, W., Morgan, J.J., 1980. Kinetics and product of ferrous iron oxygenation in aqueous systems. Environ. Sci. Technol. 14 (5), 561–568.
Tamura, H., Goto, K., Nagayama, M., 1976. The effect of ferric hydroxide on the oxygenation of ferrous ions in neutral solutions. Corros. Sci. 16 (4), 197–207.
Weiss, J.W., Rentz, J., Plaia, T.W., Neubauer, S., Merrill-Floyd, M., Lilburn, T., Bradburne, C., Megonigal, J., Emerson, D., 2007. Characterization of Neutrophilic Fe (II)-Oxidizing Bacteria Isolated from the Rhizosphere of Wetland Plants and Description of *Ferritrophicum radicicola* gen. Nov. Sp. Nov., and Sideroxydans Paludicola Sp. Geomicrob. J. 24 (7–8), 559–570.
Zeitvogel, F., Obst, M., 2016. ScatterJn: An ImageJ Plugin for Scatterplot-Matrix Analysis and Classification of Spatially Resolved Analytical Microscopy Data. J. Open Res. Softw. 4 (1).
Zeitvogel, F., Schmid, G., Hao, L., Ingino, P., Obst, M., 2016. ScatterJ: An ImageJ plugin for the evaluation of analytical microscopy datasets. J. Microsc. 261 (2), 148–156.
Zhang, Y., 2008. Geochemical Kinetics. Princeton Univ. Press, Princeton.
Zhou, N., Luther, G.W., Chan, C.S., 2021. Ligand Effects on Biotic and Abiotic Fe(II) Oxidation by the Microaerophile *Sideroxydans lithotrophicus*. Environ. Sci. Technol. 55 (13), 9362–9371.